ROYAL SOCIETY
OF CHEMISTRY

PAPER

Check for updates

Structural and optoelectronic characteristics of β-Ga₂O₃ epitaxial films with Zn alloying and subsequent oxygen annealing†

Xuan Sun,[ab] Kewei Liu, [ID] *[ab] Xing Chen,[ab] Qichao Hou,[ab] Zhen Cheng,[a] Jialin Yang,[a] Qiu Ai, [ID] [a] Yongxue Zhu, [ID] [a] Binghui Li,[ab] Lei Liu [ID] [ab] and Dezhen Shen*[ab]

Pure and ∼7.5 at% Zn alloyed β-Ga₂O₃ epitaxial films were epitaxially grown by metal organic chemical vapor deposition choosing sapphire (*c*-plane) as substrates, followed by 600 °C annealing in an oxygen atmosphere. We have characterized the structural, optical and electrical properties of the four prepared samples including as-grown pure β-Ga₂O₃, annealed pure β-Ga₂O₃, as-grown β-Ga₂O₃:Zn and annealed β-Ga₂O₃:Zn films in detail. Furthermore, solar-blind UV photodetectors with metal–semiconductor–metal structures fabricated from these epitaxial thin films have been demonstrated. A giant performance enhancement can be observed for β-Ga₂O₃ photodetectors by Zn alloying and subsequent oxygen annealing. The device fabricated from the annealed β-Ga₂O₃:Zn film shows a low dark current of ∼3.7 × 10⁻¹¹ A, a high responsivity of 2.8 × 10³ A W⁻¹ and a high UV-vis rejection ratio of 5.6 × 10⁵ at 10 V bias. And an ultra-high specific detectivity up to 5.9 × 10¹⁶ cm Hz¹ᐟ² W⁻¹ (Jones) is observed. Such excellent photodetection performance of annealed Ga₂O₃:Zn devices can be explained by the donor compensation effect and the deep level trap removal effect by the introduction of Zn. Our findings contribute a roadmap for realizing high-performance Ga₂O₃-based solar-blind photodetectors, and provide a sturdy foundation for future applications.

Introduction

Ultra-wide bandgap gallium oxide (Ga₂O₃), with remarkable thermal and chemical stability, is suitable for many promising areas of applications, such as solar-blind photodetectors, gas sensors, solar cells, power electronic devices, and so on.[1–7] There are six different crystalline structures of Ga₂O₃, including α-, β-, γ-, δ-, ε- and κ-Ga₂O₃.[8–10] In comparison, the most stable phase among them is monoclinic β-Ga₂O₃ with a direct bandgap of ∼4.9 eV.[11,12] Because of the oxygen vacancy donors, the intrinsic β-Ga₂O₃ shows n-type conductivity.[13–15] It has been shown that impurities can have a decisive influence on the physical and chemical properties of semiconductor materials by theoretical research and experimental research.[16–18] Therefore,

the doping and/or alloying technology should be an effective choice to adjust the performances in many aspects of β-Ga₂O₃ films, thereby leading to a breakthrough in β-Ga₂O₃ devices, which has attracted more and more attention.[19–21] Stannum, silicon and germanium are commonly selected as available n-type dopants, and n-type β-Ga₂O₃ with high electron concentration has been successfully achieved by doping them.[3,22–25] In contrast, lots of researchers have investigated Zn, Mg and Cu as potential p-type dopants, but they have not achieved much success due to the deep acceptor energy levels.[14,26,27] Still, it is noteworthy that doping with Zn, Mg or Cu could transform Ga₂O₃ from a conductive state to a semi-insulating state due to both the suppression of oxygen vacancy defects and the donor compensation effect.[28,29] In particular, owing to the similar ion sizes between Zn²⁺ and Ga³⁺, Zn doped/alloyed β-Ga₂O₃ has been comprehensively investigated recently.[30] Chikoidze *et al.* realized the ultra-high critical electrical field of Ga₂O₃ films by doping 0.5% Zn.[31] Guo *et al.* grew single phase Ga₂O₃:Zn thin films with Zn components from 0.69% to 3.03% and found that 3.03% Zn doped films exhibit better solar-blind UV photodetection performance.[26] Moreover, single-phase high-component Zn-doped/alloyed Ga₂O₃ seems to have more attractive optical, electrical and photoelectric properties.[32,33] However, as the content of Zn in Ga₂O₃ increases to more than ∼5%,

ᵃ State Key Laboratory of Luminescence and Applications, Changchun Institute of Optics, Fine Mechanics and Physics, Chinese Academy of Sciences, No. 3888 Dongnanhu Road, Changchun, 130033, People's Republic of China. E-mail: liukw@ciomp.ac.cn, shendz@ciomp.ac.cn

ᵇ Center of Materials Science and Optoelectronics Engineering, University of the Chinese Academy of Sciences, Beijing 100049, People's Republic of China

the transition from Ga_2O_3 to $ZnGa_2O_4$ or two-phase coexistence can be observed obviously, which makes its performance worse.[34] Till now, there have been few studies on single-phase Ga_2O_3:Zn materials with high Zn content, and most of the reported components are less than 4%.[32,35]

In this work, we report the epitaxial growth of single phase $β$-Ga_2O_3 films without and with $\sim$7.5 at% Zn alloying by metal organic chemical vapor deposition (MOCVD) on sapphire (c-plane) substrates. The composition of these films was evaluated by X-ray energy dispersive spectroscopy (EDS) as shown in Fig. S1 (ESI†). The pure $β$-Ga_2O_3 and $β$-Ga_2O_3:Zn films were characterized and investigated with and without 600 °C oxygen annealing. And the metal–semiconductor–metal (MSM) detectors based on these thin films have been demonstrated on our previously prepared samples. Among these detectors, the device based on annealed $β$-Ga_2O_3:Zn films shows the greatest comprehensive photodetection properties with a high specific detectivity of 5.9×10^{16} cm $Hz^{1/2}$ W^{-1} (Jones). We then discussed the detailed physical mechanisms of this phenomenon. Our findings suggest that single-phase high Zn content $β$-Ga_2O_3 has great potential in preparing high-performance solar-blind UV photodetectors.

Experimental section

The pure and $\sim$7.5 at% Zn alloyed $β$-Ga_2O_3 epitaxial films were prepared by MOCVD on sapphire (c-plane) substrates. Oxygen gas, triethylgallium (TEGa), and diethylzinc (DEZn) were selected as the oxygen, gallium, and zinc precursors, respectively. In the choice of carrier gas, we used high-purity nitrogen gas. The flow velocity of TEGa, DEZn and oxygen were kept at 10, 1 and 180 standard cubic centimeter per minute (sccm), respectively. TEGa and DEZn bubblers were kept at 10 and −9 °C, respectively. The growth conditions have been optimized, and the films were grown at a 680 °C substrate temperature and a 3000 Pa chamber pressure. After 90 minutes of epitaxial growth, the prepared samples were annealed for 120 min at a temperature of 600 °C in an O_2 atmosphere. The crystal structure was measured using a Bruker D8GADDS X-ray diffractometer (XRD) with the radiation source of Cu Kα ($λ = 0.154$ nm). The optical properties and the morphological properties of films were investigated using an UV-3101PC scanning spectrophotometer and a scanning electron microscope (SEM) (HITACHI S-4800), respectively. The chemical composition of the films was measured by X-ray photoelectron spectroscopy (XPS). Raman spectra were recorded using a DU970P-BVF spectral detector at room temperature.

To further explore the photodetection function of the $β$-Ga_2O_3 films without and with Zn alloying, photolithography and lift-off processes were carried out to fabricate Au interdigital electrodes on these films, thus realizing MSM photodetectors. The time-dependent photocurrent (I–t) curves and current–voltage (I–V) characteristic curves of the devices were determined using a semiconductor device analyser (Agilent B1500A). The photoresponse of the detectors was tested using

a monochromator with an UV-enhanced Xe lamp of 200 W as the source of light.

Results and discussion

The XRD patterns of pure and Zn alloyed $β$-Ga_2O_3 epitaxial films with and without annealing are shown in Fig. 1a. The sharp and strong peak at $2θ = 41.68°$ can be identified to be the (0006) diffraction plane of the substrate we used (c-face sapphire). Obviously, similar XRD patterns are shown for the four samples, and only three diffraction peaks located at $2θ = \sim$19.0°, $\sim$38.2°, and $\sim$59.0° can be observed, which corresponds to the (−201), (−402) and (−603) diffraction planes of the monoclinic structured $β$-Ga_2O_3 (JCPDS No. 043–1012), respectively. After Zn alloying, no new diffraction peaks appeared, but the intensities of the (−201), (−402) and (−603) peaks are obviously weakened. Moreover, the ratio of the intensity of the (−201) peak to that of the (−402) peak decreases obviously after the introduction of Zn into Ga_2O_3. These phenomena indicate that the crystalline quality of Ga_2O_3 is obviously reduced after Zn alloying, but no obvious change is found in the structure.[22] Normalized (−201) diffraction peaks are shown in Fig. 1b, and a slight shift towards lower $2θ$ angle can be clearly observed. This is due to the fact that the radius of the Ga^{3+} ion (0.61 Å) is slightly smaller than that of the Zn^{2+} ion (0.74 Å).[36] When Zn^{2+} with a larger radius is in the substitutional position of Ga^{3+}, it will lead to lattice expansion, which is manifested as a smaller angle shift of the XRD diffraction peak. Besides, when Zn is in the interstitial position, the lattice will also expand.

Fig. 1c shows the optical transmission properties of our samples. In the wavelength range from 300 to 800 nm, the average transmittance is over 85% of each sample. Furthermore, steep absorption edges can be clearly observed at $\sim$255 nm. According to the plots of $(αhν)^2$ versus $hν$ in the inset of Fig. 1c, the optical bandgap (E_g) of pure $β$-Ga_2O_3, $β$-Ga_2O_3:Zn, annealed $β$-Ga_2O_3 and annealed $β$-Ga_2O_3:Zn can be evaluated to be 5.23, 5.21, 5.19, and 5.15 eV, respectively. The calculated optical bandgap of $β$-Ga_2O_3 is slightly reduced after alloying and annealing, which may be associated with the change in lattice stress.[37]

The cross-sectional and the top-view SEM images of pure and Zn-alloyed $β$-Ga_2O_3 with and without annealing at 600 °C in an oxygen atmosphere are shown in Fig. 2. It is obvious that the thickness of all four samples is about 230 nm. In addition, the grain size on the surface of Ga_2O_3 thin films is obviously reduced after Zn alloying.

As shown in Fig. S2 (ESI†) and Fig. 3, to analyse the chemical characterization of these samples, XPS characterization has been performed on pure $β$-Ga_2O_3 and $β$-Ga_2O_3:Zn films without and with annealing. Fig. 3a exhibits the high-resolution Ga 2p core-level spectra of the four samples. According to previous reports, the peaks at 1117.85 eV and 1144.7 eV can be associated with Ga $2p^{3/2}$ and Ga$2p^{1/2}$, respectively.[38,39] The spin-orbit splitting of 26.85 eV can be observed, corresponding to $β$-Ga_2O_3.[40] After Zn alloying and/or annealing, no obvious
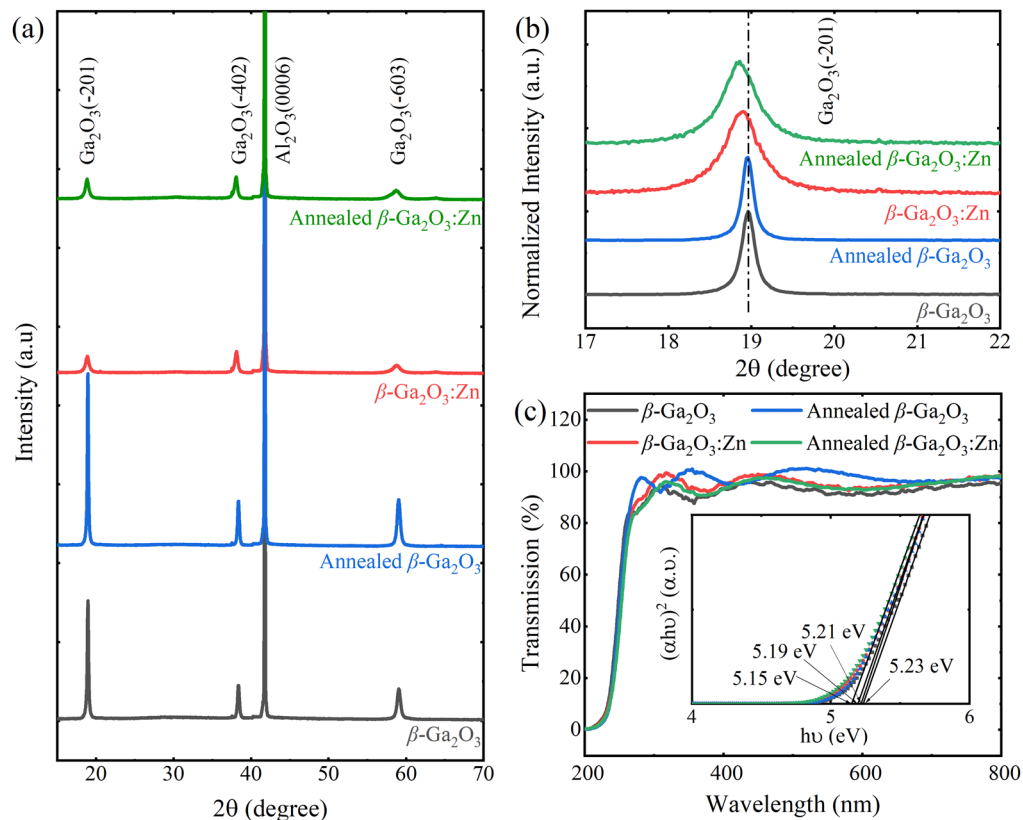
3228 | J. Mater. Chem. C, 2023, **11**, 3227–3234

This journal is © The Royal Society of Chemistry 2023

Fig. 1 (a) XRD patterns, (b) normalized (−201) diffraction peaks, and (c) optical transmission spectra of pure β-Ga_2O_3 and β-Ga_2O_3:Zn films with and without annealing. Plots of $(\alpha h\nu)^2$ against $h\nu$ for the films are shown in the inset of (c).
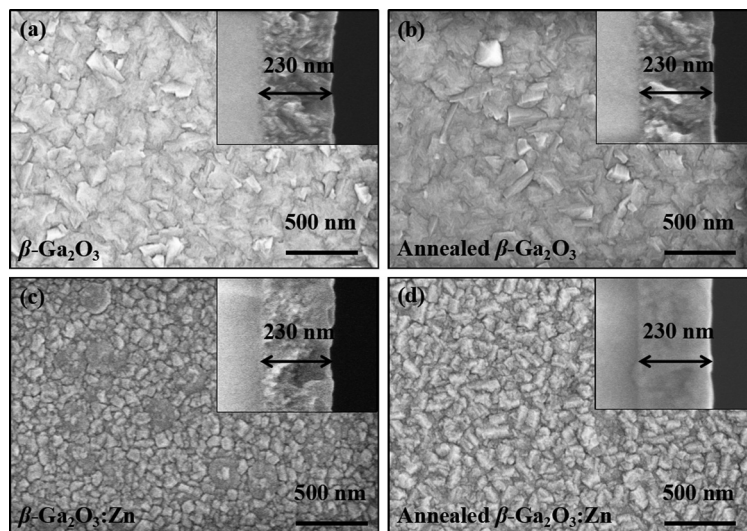

Fig. 2 SEM images of pure β-Ga_2O_3 (a), annealed β-Ga_2O_3 (b), β-Ga_2O_3:Zn (c), and annealed β-Ga_2O_3:Zn films (d).

change can be found in the Ga 2p XPS spectra. Fig. 3b shows the high-resolution Zn $2p_{3/2}$ core-level spectra of Zn-alloyed β-Ga_2O_3 thin films without and with annealing. The Zn $2p^{3/2}$ core-level spectra could be fitted by two peaks, which are respectively located at 1021.6 and 1022.1 eV. The constituent (Zn_A) at lower binding energy (BE) could be attributed to the Zn–O bonds and the higher BE constituent (Zn_B) can be ascribed to the Zn interstitials.[41] Obviously, Zn substitution on the Ga sites (Zn_{Ga}) and Zn interstitial atoms coexist in the as-grown Ga_2O_3:Zn film. After high-temperature oxygen

This journal is © The Royal Society of Chemistry 2023
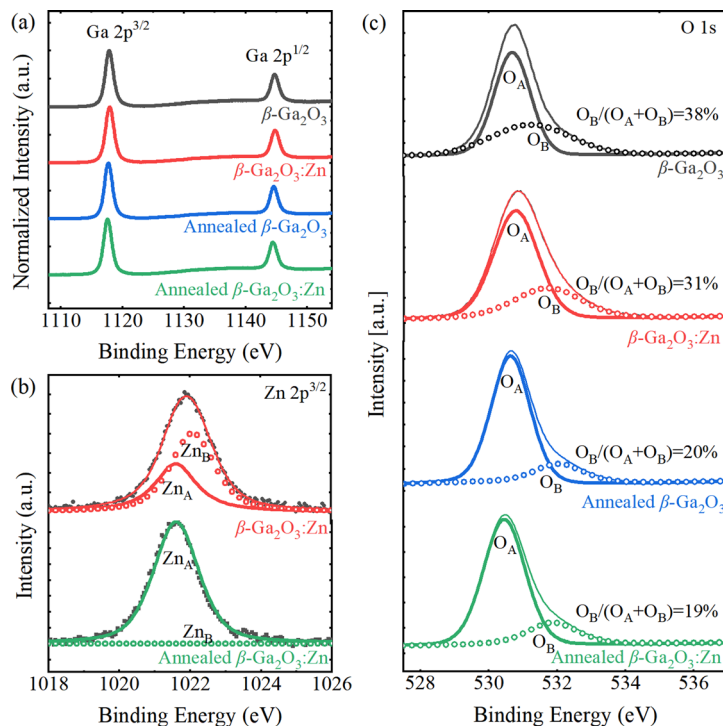
J. Mater. Chem. C, 2023, 11, 3227–3234 | 3229

Fig. 3 High-resolution XPS spectra of (a) Ga 2p, and (b) Zn 2p$^{3/2}$, and (c) O 1s core-level spectra of pure β-Ga$_2$O$_3$ and β-Ga$_2$O$_3$:Zn films without and with annealing.

annealing, the signal of Zn$_B$ almost completely disappears, illustrating that all Zn impurities are efficiently introduced in the lattice and turn into a part of chemical bonding.

Fig. 3c shows the XPS spectra of high-resolution O 1s core-level of the samples. Obviously, two nearly Gaussian components could be used to fit the O 1s peak. The peak which was located at about 530.5 eV (O$_A$) can be assigned to lattice oxygen (O^{2-}), while the 531.5 eV (O$_B$) peak is related to oxygen vacancies.[42] It can be seen that the formation of oxygen vacancies could be inhibited by the introduction of Zn into β-Ga$_2$O$_3$. In addition, 600 °C annealing in an oxygen atmosphere could provide oxygen atoms to fill the oxygen vacancies, resulting in the significant reduction of oxygen vacancies in β-Ga$_2$O$_3$ with and without Zn.

The room temperature Raman spectra ranging from 100 cm^{-1} to 900 cm^{-1} of pure β-Ga$_2$O$_3$ and β-Ga$_2$O$_3$:Zn films without and with annealing and sapphire are presented in Fig. 4. Except for the signals from the sapphire substrate, the Raman peaks related to the β-Ga$_2$O$_3$ can be divided into three categories: high-frequency sections at 661.5 cm^{-1} and 770.1 cm^{-1} are ascribed to the stretching and bending vibration modes of GaO$_4$; medium frequency sections at 351.0 cm^{-1} and 480.7 cm^{-1} are associated with the GaO$_6$ bending vibration modes; the low-frequency sections at 147.4 cm^{-1}, 172.0 cm^{-1} and 203.6 cm^{-1} can be pertained to the vibration and translation modes of the GaO$_4$–GaO$_6$ chains.[43,44] After Zn alloying, due to the local strain caused by the introduction of impurities, the intensity of all peaks becomes weak, and some even disappear completely.[45,46]
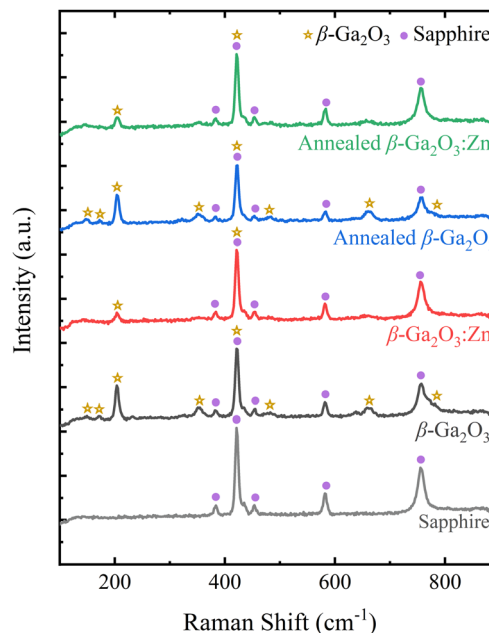

Fig. 4 Raman spectra of pure and Zn-alloyed β-Ga$_2$O$_3$ films without and with annealing and sapphire substrate at room temperature.

To examine the solar-blind UV photodetection properties of these films, we constructed MSM detectors consisting of twenty-five pairs of gold interdigitated electrodes (thickness controlled at ~50 nm) using photolithography and lift-off processes. The device structure is schematically shown in Fig. 5a. Fig. 5b and c present
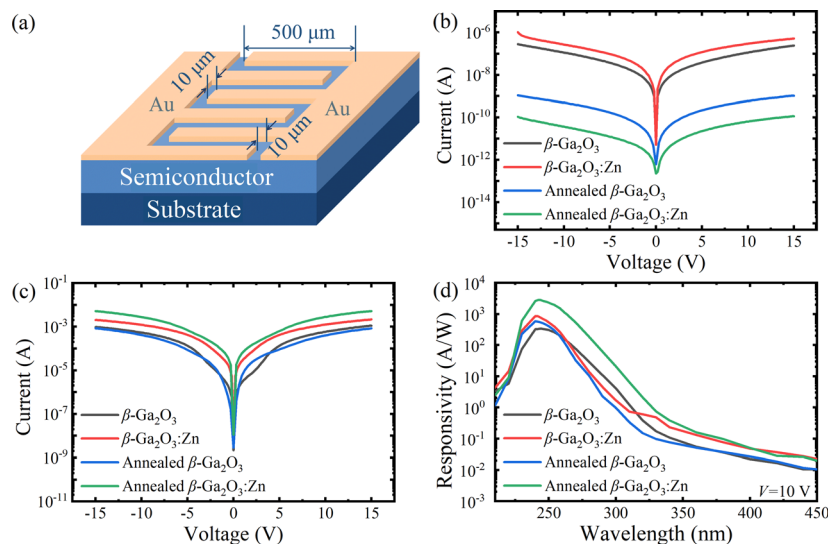
3230 | *J. Mater. Chem. C*, 2023, **11**, 3227–3234

This journal is © The Royal Society of Chemistry 2023

Fig. 5 (a) MSM device structure schematic diagram. *I–V* curves of the devices in the dark (b) and under illumination of 254 nm UV light (c). (d) The spectral response of the photodetectors.

the *I–V* curves of the devices in the dark and under illumination of 254 nm UV light, respectively. In Fig. 5b, it can be found that Zn alloying could slightly increase the dark current of the β-Ga$_2$O$_3$ photodetector, which may be associated with the Zn interstitial related donors. After annealing in oxygen, the dark currents of both pure β-Ga$_2$O$_3$ and β-Ga$_2$O$_3$:Zn photodetectors decreased significantly due to the reduction of oxygen vacancy donors. Moreover, all donor-type Zn interstitials in β-Ga$_2$O$_3$:Zn have been converted to acceptor-type Zn substitution Ga, and thus the reduction of donors and the compensation effect of Zn$_{Ga}$ deep level acceptors further decreased the dark current to 37 pA at 10 V. As shown in Fig. 5c, the current of all four devices exhibits a significant increase under 254 nm UV light illumination (650 μW cm^{-2}). Interestingly, among these four devices, the annealed β-Ga$_2$O$_3$:Zn photodetectors have the largest photocurrent of ∼2.7 mA at 10 V bias.

The photoresponse spectra of the detectors are shown in Fig. 5d at 10 V bias. The response peaks appeared at ∼245 nm for all devices with −3 dB cutoff edges of 254 nm, which corresponds to the calculated bandgap energies of the films. In addition, the highest peak responsivity (R_{peak}) of 2.8×10^3 A W^{-1} among them can be observed in the annealed Ga$_2$O$_3$:Zn device with a UV-visible rejection ratio (R_{peak}/R_{400nm}) of 5.6×10^5, indicating high gain and excellent intrinsic solar blindness. Furthermore, the specific detectivity (D^*) is also a crucial parameter for a photodetector, which is calculated to be 5.9×10^{16} cm Hz$^{1/2}$ W^{-1} (Jones) for the device based on annealed Ga$_2$O$_3$:Zn using the following equations:[47]

$$D^* = \sqrt{A \Delta f} \Big/ \text{NEP} \quad (1)$$

$$\text{NEP} = I_n \big/ R \quad (2)$$

where A is the effective area of the device, Δf is the electrical bandwidth, NEP is the noise equivalent power, I_n is the noise

current and R is the responsivity. Typically, for a MSM UV photodetector, dark noise (shot noise) is usually regarded as the main source of noise.[48,49]

To further investigate the photoresponse properties of MSM photodetectors fabricated from pure β-Ga$_2$O$_3$, annealed β-Ga$_2$O$_3$, β-Ga$_2$O$_3$:Zn, and annealed β-Ga$_2$O$_3$:Zn films, the time-dependent current characteristic measurement has been carried out under illumination of 254 nm light at 10 V bias (see Fig. S3, ESI†). And the light power densities were between 0.7 and 630 μW cm^{-2}. Under several different light power densities, all the photodetectors present excellent ON/OFF switching performance, reflecting good repeatability and stability. Fig. 6 presents the relationship between the photocurrent and the incident illumination intensities at 10 V bias of our four devices. The photocurrent *versus* illumination intensity could be fitted by the power law relationship:[50]

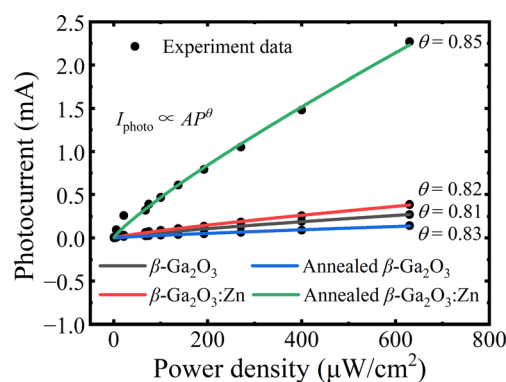$$I_{photo} \propto AP^{\theta} \quad (3)$$

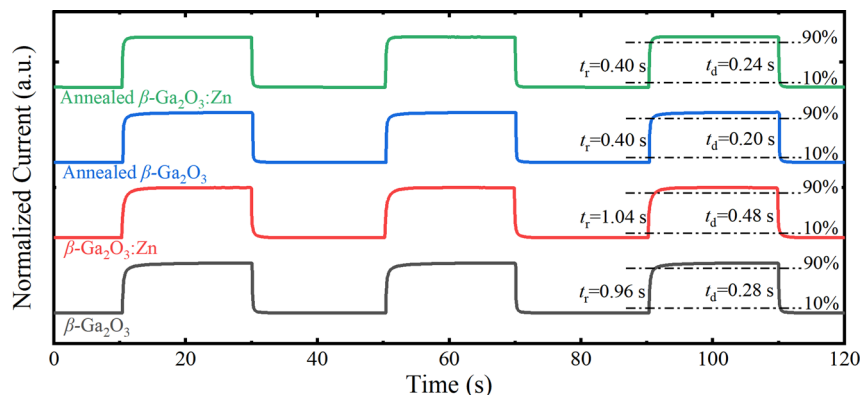**Fig. 6** The function relationship between the photocurrent and illumination intensity.

This journal is © The Royal Society of Chemistry 2023

J. Mater. Chem. C, 2023, **11**, 3227–3234 | **3231**

Fig. 7 I–t curves of pure and Zn-alloyed β-Ga$_2$O$_3$ films without and with annealing.

where P is the light intensity, A is a constant and the θ is a parameter that reflects the trapping and recombination of the photo-induced carriers of photodetectors. As we can see, the fitting result shows a nearly linear behaviour for all four detectors, and the θ values is calculated to be 0.81, 0.82, 0.83 and 0.85 for pure β-Ga$_2$O$_3$, annealed β-Ga$_2$O$_3$, β-Ga$_2$O$_3$:Zn, and annealed β-Ga$_2$O$_3$:Zn photodetectors, respectively. Clearly, Zn alloying and oxygen annealing could slightly increase the θ values of the devices, which can be explained by the contribution of more photogenerated carriers to the photocurrent and the reduced trapping and recombination. In addition, this is also the main reason why the annealed β-Ga$_2$O$_3$:Zn device has the highest responsivity as shown in Fig. 5d.

To examine the response speed of the device, we tested the I–t curves of the devices at 10 V bias under 254 nm UV light illumination (650 μW cm^{-2}) as shown in Fig. 7. Obviously, all four devices exhibit excellent reproducibility and stability with quick response speed. Moreover, the 10–90% increase and 90–10% decay times (t_r, t_d) are estimated to be (0.96 s, 0.28 s), (1.04 s, 0.48 s), (0.40 s, 0.20 s), and (0.40 s, 0.24 s) for the devices based on as-grown β-Ga$_2$O$_3$, as-grown β-Ga$_2$O$_3$:Zn, annealed β-Ga$_2$O$_3$ and annealed β-Ga$_2$O$_3$:Zn films, respectively. It can be found that the Zn alloying could slightly slow down the response speed of β-Ga$_2$O$_3$ photodetectors. In addition, high

temperature annealing in an oxygen atmosphere can reduce the response time to some extent.

Table 1 shows the comparison between our annealed Zn-alloyed Ga$_2$O$_3$ device and some reported solar-blind photodetectors fabricated from Ga$_2$O$_3$ thin films. In comparison, our device shows a superior solar-blind photodetection performance, implying that the combination of ∼7.5 at% Zn alloying and high-temperature oxygen annealing is an effectual method to realize excellent β-Ga$_2$O$_3$ solar-blind UV photodetectors.

Conclusions

In a word, β-Ga$_2$O$_3$ and β-Ga$_2$O$_3$:Zn epitaxial films have been prepared on sapphire (c-face) by MOCVD with and without subsequent 600 °C annealing in an oxygen atmosphere. The experimental results illustrate that β-Ga$_2$O$_3$:Zn films with a Zn content of ∼7.5 at% still maintained a single monoclinic structure. More interestingly, the MSM solar-blind UV photodetector fabricated from an annealed β-Ga$_2$O$_3$:Zn film exhibits a superior performance to the devices based on other films. A low dark current (3.7×10^{-11} A), a high photoresponse (2.8×10^3 A W^{-1}) and a large UV-visible rejection (5.6×10^5) can be observed for the annealed β-Ga$_2$O$_3$:Zn photodetector at 10 V.

Table 1 Performance comparison of various solar-blind photodetectors based on Ga$_2$O$_3$ films

Materials	Voltage (V)	Dark current (pA)	Responsivity (A W^{-1})	UV-vis rejection ratio	Detectivity (Jones)	Ref.
a-Ga$_2$O$_3$	20	9.2	1099	9	—	51
a-GaO$_x$	12	0.046	66.7	1.8×10^7	8×10^{15}	52
ε-Ga$_2$O$_3$	6	23.5	230	1.2×10^5	1.2×10^{15}	53
β-Ga$_2$O$_3$	−40	—	1.2×10^5	>10^5	2×10^{16}	54
β-Ga$_2$O$_3$	5	∼6×10^5	96.13	>10^2	—	55
β-Ga$_2$O$_3$	10	0.082	1.93	>10^2	6.53×10^{13}	56
β-Ga$_2$O$_3$	10	0.1	29.8	9460	1.5×10^{12}	57
β-Ga$_2$O$_3$	20	0.15	46	3.7×10^7	9.8×10^{15}	58
β-Ga$_2$O$_3$	20	∼0.5	371	1.1×10^8	6.6×10^{16}	59
β-Ga$_2$O$_3$:Zn	10	1.45	∼0.3	—	—	60
β-Ga$_2$O$_3$:Zn	5	16	1.05	—	4.9×10^{11}	61
β-Ga$_2$O$_3$:Zn	20	∼10	210	5×10^4	—	62
β-Ga$_2$O$_3$:Zn	10	310	—	—	—	32
β-Ga$_2$O$_3$:Zn	10	37	2.8×10^3	5.6×10^5	5.9×10^{16}	This work

The excellent photodetection performance of the annealed β-Ga$_2$O$_3$:Zn device may be derived from the donor compensation effect and the deep level trap removal effect by the introduction of Zn. And the suppression of oxygen vacancy donors by the introduction of Zn and subsequent oxygen annealing should be another important reason. The present studies and results provide guidance for obtaining high performance Ga$_2$O$_3$-based solar-blind photodetectors.

Author contributions

The manuscript was written through contributions from all authors. Xuan Sun: investigation and writing – original draft. Kewei Liu: validation, formal analysis, writing – review & editing, supervision, and resources. Xing Chen: resources and visualization. Qichao Hou: visualization. Zhen Cheng: Raman analyses. Jialin Yang: supervision. Qiu Ai: supervision. Yongxue Zhu: supervision. Binghui Li: resources and supervision. Lei Liu: resources and supervision. Dezhen Shen: supervision and resources. All authors have given approval to the final version of the manuscript.

Conflicts of interest

The authors declare no competing financial interest.

Acknowledgements

References

1 J. Yang, K. Liu, X. Chen and D. Shen, *Prog. Quantum Electron.*, 2022, **83**, 100397.

2 H. Bae, K.-S. Lee, P. D. Ye and J.-Y. Park, *Solid-State Electron.*, 2021, **185**, 108134.

3 R. Pilliadugula and N. Gopalakrishnan, *Mater. Sci. Semicond. Process.*, 2021, **135**, 106086.

4 H. Wang, J. Ma, L. Cong, H. Zhou, P. Li, L. Fei, B. Li, H. Xu and Y. Liu, *Mater. Today Phys.*, 2021, **20**, 100464.

5 Y. Liang, M. Ma, X. Zhong, C. Xie, X. Tong, K. Xing and C. Wu, *IEEE Electron Device Lett.*, 2021, **42**(8), 1192–1195.

6 D. Y. Guo, K. Chen, S. L. Wang, F. M. Wu, A. P. Liu, C. R. Li, P. G. Li, C. K. Tan and W. H. Tang, *Phys. Rev. Appl.*, 2020, **13**(2), 024051.

7 B. S. Qiao, Z. Z. Zhang, X. H. Xie, B. H. Li, X. Chen, H. F. Zhao, K. W. Liu, L. Liu and D. Z. Shen, *J. Mater. Chem. C*, 2021, **9**(11), 4039–4045.

8 S. J. Pearton, J. Yang, P. H. Cary, F. Ren, J. Kim, M. J. Tadjer and M. A. Mastro, *Appl. Phys. Rev.*, 2018, **5**(1), 011301.

9 C. Xie, X. T. Lu, X. W. Tong, Z. X. Zhang, F. X. Liang, L. Liang, L. B. Luo and Y. C. Wu, *Adv. Funct. Mater.*, 2019, **29**(9), 1806006.

10 C. Wu, F. Wu, H. Hu, S. Wang, A. Liu and D. Guo, *Mater. Today Phys.*, 2022, **28**, 100883.

11 C. Xie, X. Lu, Y. Liang, H. Chen, L. Wang, C. Wu, D. Wu, W. Yang and L. Luo, *J. Mater. Sci. Technol.*, 2021, **72**, 189–196.

12 V. I. Nikolaev, A. I. Pechnikov, S. I. Stepanov, S. S. Sharofidinov, A. A. Golovatenko, I. P. Nikitina, A. N. Smirnov, V. E. Bugrov, A. E. Romanov, P. N. Brunkov and D. A. Kirilenko, *Semiconductors*, 2016, **50**(7), 980–983.

13 L. Dong, R. Jia, B. Xin and Y. Zhang, *J. Vac. Sci. Technol., A*, 2016, **34**(6), 060602.

14 Q. Feng, J. Liu, Y. Yang, D. Pan, Y. Xing, X. Shi, X. Xia and H. Liang, *J. Alloys Compd.*, 2016, **687**, 964–968.

15 Y. Zhang, J. Yan, Q. Li, C. Qu, L. Zhang and T. Li, *Phys. B*, 2011, **406**(15–16), 3079–3082.

16 J. Wang, M. Wang, F. Xu, B. Liu, J. Lang, N. Zhang, X. Kang, Z. Qin, X. Yang, X. Wang, W. Ge and B. Shen, *Light: Sci. Appl.*, 2022, **11**(1), 71–78.

17 T. Ymanaka, Y. Hayashi and H. Takizawa, *Ultrason. Sonochem.*, 2022, **89**, 106114.

18 Q. Cai, H. You, H. Guo, J. Wang, B. Liu, Z. Xie, D. Chen, H. Lu, Y. Zheng and R. Zhang, *Light: Sci. Appl.*, 2021, **10**(1), 94.

19 X. Cai, F. P. Sabino, A. Janotti and S.-H. Wei, *Phys. Rev. B*, 2021, **103**(11), 115205.

20 M. M. Chang, J. H. Ye, Y. L. Su, J. Q. Shen, N. Zhao, J. B. Wang, H. J. Song, X. L. Zhong, S. L. Wang, W. H. Tang and D. Y. Guo, *J. Phys. D: Appl. Phys.*, 2022, **55**(3), 035103.

21 G. Pozina, C.-W. Hsu, N. Abrikossova and C. Hemmingsson, *Phys. Status Solidi A*, 2021, **218**(21), 2100486.

22 S. H. Jeong, T. K. O. Vu and E. K. Kim, *J. Alloys Compd.*, 2021, **877**, 106291.

23 D. Guo, Y. Su, H. Shi, P. Li, N. Zhao, J. Ye, S. Wang, A. Liu, Z. Chen, C. Li and W. Tang, *ACS Nano*, 2018, **12**(12), 12827–12835.

24 C.-C. Wang, B.-C. Lee, F.-S. Shieu and H. C. Shih, *Chem. Phys. Lett.*, 2020, **753**, 137624.

25 E. Ahmadi, O. S. Koksaldi, S. W. Kaun, Y. Oshima, D. B. Short, U. K. Mishra and J. S. Speck, *Appl. Phys. Express*, 2017, **10**(4), 041102.

26 A. Kyrtsos, M. Matsubara and E. Bellotti, *Appl. Phys. Lett.*, 2018, **112**(3), 032108.

27 J. Sun and J. Leng, *Phys. B*, 2019, **552**, 195–201.

28 S. Bhandari, J. L. Lyons, D. Wickramaratne and M. E. Zvanut, *APL Mater.*, 2022, **10**(2), 021103.

29 J. Jesenovec, C. Pansegrau, M. D. McCluskey, J. S. McCloy, T. D. Gustafson, L. E. Halliburton and J. B. Varley, *Phys. Rev. Lett.*, 2022, **128**(7), 077402.

30 H. Abdullah, R. T. Ginting, A. C. Sembiring, N. S. Gultom, H. Shuwanto and D.-H. Kuo, *New J. Chem.*, 2021, **45**(42), 19889–19902.

31 E. Chikoidze, T. Tchelidze, C. Sartel, Z. Chi, R. Kabouche, I. Madaci, C. Rubio, H. Mohamed, V. Sallet, F. Medjdoub, A. Perez-Tomas and Y. Dumont, *Mater. Today Phys.*, 2020, **15**, 100263.

32 D. Guo, X. Qin, M. Lv, H. Shi, Y. Su, G. Yao, S. Wang, C. Li, P. Li and W. Tang, *Electron. Mater. Lett.*, 2017, **13**(6), 483–488.

33 X. L. Zhao, Z. P. Wu, Y. S. Zhi, Y. H. An, W. Cui, L. H. Li and W. H. Tang, *J. Phys. D: Appl. Phys.*, 2017, **50**(8), 085102.

34 E. Chikoidze, C. Sartel, I. Madaci, H. Mohamed, C. Vilar, B. Ballesteros, F. Belarre, E. Elena del Corro, P. Vales-Castro, G. Sauthier, L. Li, M. Jennings, V. Sallet, Y. Dumont and A. Pérez-Tomás, *Cryst. Growth Des.*, 2020, **20**(4), 2535–2546.

35 I. López, M. Alonso-Orts, E. Nogales and B. Méndez, *Phys. Status Solidi A*, 2018, **215**(19), 1800217.

36 S. S. Gao, W. X. Li, J. F. Dai, Q. Wang and Z. Q. Suo, *Mater. Res. Express*, 2021, **8**(2), 025904.

37 H. Zhang, J. X. Deng, L. Kong, Z. Pan, Z. Bai and J. Wang, *Micro Nano Lett.*, 2019, **14**(1), 62–65.

38 L. A. M. Lyle, T. C. Back, C. T. Bowers, A. J. Green, K. D. Chabak, D. L. Dorsey, E. R. Heller and L. M. Porter, *APL Mater.*, 2021, **9**(6), 061104.

39 S. Acikgoz and H. Yungevis, *Appl. Phys. A: Mater. Sci. Process.*, 2020, **126**(8), 644–656.

40 D. A. Zatsepin, D. W. Boukhvalov, A. F. Zatsepin, Y. A. Kuznetsova, D. Gogova, V. Y. Shur and A. A. Esin, *Superlattices Microstruct.*, 2018, **120**, 90–100.

41 Y. Y. Chen, J. C. Hsu, C. Y. Lee and P. W. Wang, *J. Mater. Sci.*, 2013, **48**(3), 1225–1230.

42 S. Han, X. L. Huang, M. Z. Fang, W. G. Zhao, S. J. Xu, D. L. Zhu, W. Y. Xu, M. Fang, W. J. Liu, P. J. Cao and Y. M. Lu, *J. Mater. Chem. C*, 2019, **7**(48), 15383.

43 B. M. Janzen, P. Mazzolini, R. Gillen, A. Falkenstein, M. Martin, H. Tornatzky, J. Maultzsch, O. Bierwagen and M. R. Wagner, *J. Mater. Chem. C*, 2021, **9**(7), 2311–2320.

44 P. Li, X. Han, D. Chen, Q. Sai and H. Qi, *CrystEngComm*, 2022, **24**(31), 5588–5596.

45 H. Cui, H. F. Mohamed, C. Xia, Q. Sai, W. Zhou, H. Qi, J. Zhao, J. Si and X. Ji, *J. Alloys Compd.*, 2019, **788**, 925–928.

46 T. Onuma, S. Fujioka, T. Yamaguchi, Y. Itoh, M. Higashiwaki, K. Sasaki, T. Masui and T. Honda, *J. Cryst. Grow.*, 2014, **401**, 330–333.

47 Y. Fang, A. Armin, P. Meredith and J. Huang, *Nat. Photonics*, 2018, **13**(1), 1–4.

48 M. Zumuukhorol, Z. Khurelbaatar, S.-H. Yuk, J. Won, S.-N. Lee and C.-J. Choi, *Microelectron. Reliab.*, 2017, **69**, 60–65.

49 X. Luo, S. Chen, L. Liu, J. Lv, A. Qadir, K. Shehzad, X. Qiao, Y. Xu, L. Kienle, A. Lotnyk, X. Zhang, G. Qian and X. Fan, *J. Phys. Chem. C*, 2018, **123**(1), 810–816.

50 L. Zeng, D. Wu, J. Jie, X. Ren, X. Hu, S. P. Lau, Y. Chai and Y. H. Tsang, *Adv. Mater.*, 2020, **32**(52), 2004412.

51 H. Zhou, L. Cong, J. Ma, B. Li, M. Chen, H. Xu and Y. Liu, *J. Mater. Chem. C*, 2019, **7**(42), 13149–13155.

52 X. Hou, X. Zhao, Y. Zhang, Z. Zhang, Y. Liu, Y. Qin, P. Tan, C. Chen, S. Yu, M. Ding, G. Xu, Q. Hu and S. Long, *Adv. Mater.*, 2022, **34**(1), 2106923.

53 Y. Qin, L. Li, X. Zhao, G. S. Tompa, H. Dong, G. Jian, Q. He, P. Tan, X. Hou, Z. Zhang, S. Yu, H. Sun, G. Xu, X. Miao, K. Xue, S. Long and M. Liu, *ACS Photonics*, 2020, **7**(3), 812–820.

54 Z. Li, Y. Cheng, Y. Xu, Z. Hu, W. Zhu, D. Chen, Q. Feng, H. Zhou, J. Zhang, C. Zhang and Y. Hao, *IEEE Electron Device Lett.*, 2020, **41**(12), 1794–1797.

55 K. Arora, N. Goel, M. Kumar and M. Kumar, *ACS Photonics*, 2018, **5**(6), 2391–2401.

56 S. R. Zhou, X. Peng, H. W. Liu, Z. F. Zhang, L. J. Ye, H. L. Li, Y. Q. Xiong, L. N. Niu, F. L. Chen, L. Fang, C. Y. Kong, W. N. Li, X. Yang and H. Zhang, *Opt. Mater. Express*, 2022, **12**(1), 327–337.

57 S. Oh, C. K. Kim and J. Kim, *ACS Photonics*, 2018, **5**(3), 1123–1128.

58 B. S. Qiao, Z. Z. Zhang, X. H. Xie, B. H. Li, K. X. Li, X. Chen, H. F. Zhao, K. W. Liu, L. Liu and D. Z. Shen, *J. Phys. Chem. C*, 2019, **123**(30), 18516–18520.

59 Z. Zheng, B. Qiao, Z. Zhang, X. Huang, X. Xie, B. Li, X. Chen, K. Liu, L. Liu and D. Shen, *IEEE Trans. Electron Devices*, 2022, **69**(8), 4362–4365.

60 X. Zhao, Z. Wu, Y. Zhi, Y. An, W. Cui, L. Li and W. Tang, *J. Phys. D: Appl. Phys.*, 2017, **50**(8), 058102.

61 Y. Li, D. Zhang, R. Lin, Z. Zhang, W. Zheng and F. Huang, *ACS Appl. Mater. Interfaces*, 2019, **11**(1), 1013–1020.

62 F. Alema, B. Hertog, O. Ledyaev, D. Volovik, G. Thoma, R. Miller, A. Osinsky, P. Mukhopadhyay, S. Bakhshi, H. Ali and W. V. Schoenfeld, *Phys. Status Solidi A*, 2017, **214**(5), 1–7.

3234 | *J. Mater. Chem. C*, 2023, **11**, 3227–3234

This journal is © The Royal Society of Chemistry 2023